

Kohn–Sham decomposition in real-time time-dependent density-functional theory: An efficient tool for analyzing plasmonic excitations

Tuomas P. Rossi,^{1,*} Mikael Kuisma,^{2,3,†} Martti J. Puska,¹ Risto M. Nieminen,¹ and Paul Erhart^{2,‡}

¹*COMP Centre of Excellence, Department of Applied Physics,
Aalto University School of Science, Espoo, Finland*

²*Department of Physics, Chalmers University of Technology, Gothenburg, Sweden*

³*Department of Chemistry, Nanoscience Center, University of Jyväskylä, Jyväskylä, Finland*

(Dated: March 9, 2017)

The real-time-propagation formulation of time-dependent density-functional theory (RT-TDDFT) is an efficient method for modeling the optical response of molecules and nanoparticles. Compared to the widely adopted linear-response TDDFT approaches based on, *e.g.*, the Casida equations, RT-TDDFT appears, however, lacking efficient analysis methods. This applies in particular to a decomposition of the response in the basis of the underlying single-electron states. In this work, we overcome this limitation by developing an analysis method for obtaining the Kohn–Sham electron-hole decomposition in RT-TDDFT. We demonstrate the equivalence between the developed method and the Casida approach by a benchmark on small benzene derivatives. Then, we use the method for analyzing the plasmonic response of icosahedral silver nanoparticles up to Ag₅₆₁. Based on the analysis, we conclude that in small nanoparticles individual single-electron transitions can split the plasmon into multiple resonances due to strong single-electron–plasmon coupling whereas in larger nanoparticles a distinct plasmon resonance is formed.

PACS numbers: 31.15.ee, 71.15.Qe, 73.22.Lp, 78.67.Bf

I. INTRODUCTION

Time-dependent density-functional theory (TDDFT)¹ built on top of Kohn–Sham (KS) density-functional theory (DFT)^{2,3} is a powerful tool in computational physics and chemistry for accessing the optical properties of matter.^{4,5} Starting from seminal works on jellium nanoparticles,^{6–8} TDDFT has become a standard tool for modeling plasmonic response from a quantum-mechanical perspective,^{9,10} and proven to be useful for calculating the response of individual nanoparticles,^{11–21} and their compounds^{22–32} as well as other plasmonic materials.^{33–36} Additionally, a number of models and concepts have been developed for quantifying and understanding plasmonic character within the TDDFT framework.^{37–48} Thus, in conjunction with other theoretical and computational methods^{49–56} and experimental developments,^{57–67} TDDFT is a valuable tool for understanding quantum effects within the nanoplasmonics field.^{68,69} Recent methodological advances and a steady increase in computational power have extended the system size that can be treated at the TDDFT level, enabling the computational modeling of plasmonic phenomena in noble metal nanoparticles of several nanometers in diameter.^{70–74}

TDDFT in the linear-response regime is usually formulated in frequency space^{75,76} in terms of the Casida matrix expressed in the Kohn–Sham electron-hole space.^{75,77} The calculations are commonly performed by diagonalizing the Casida matrix directly or by solving the equivalent problem with different iterative subspace algorithms.^{78–81} The real-time-propagation formulation of TDDFT (RT-TDDFT)^{82,83} is a computationally efficient alternative to frequency-space approaches

with favorable scaling with respect to system size,⁸⁴ and has the additional advantage of being also applicable to the non-linear regime. However, RT-TDDFT results are often limited to absorption spectra or to analyses of transition densities, apart from a few exceptions focusing on characterizing plasmonic^{45–47,85} or other electronic excitations.^{86–89} In contrast, the Casida approach directly enables an extensive analysis in terms of the KS electron-hole decomposition of the excitations and thereby readily yields quantum-mechanical understanding of the plasmonic response.^{39–44,72,73,90,91}

In this work, we remedy the lack of analysis tools in RT-TDDFT and demonstrate that the decomposition of the electronic excitations in terms of the underlying KS electron-hole space can be obtained within RT-TDDFT, in equivalent fashion to the Casida approach. We have combined the analysis method with a recent RT-TDDFT implementation⁷¹ based on the linear combination of atomic orbitals (LCAO) method⁹² that is part of the open source GPAW code.^{93–95}

By using the developed method, we perform a KS decomposition analysis of the plasmon formation in a series of icosahedral silver nanoparticles comprising Ag₅₅, Ag₁₄₇, Ag₃₀₉, and Ag₅₆₁. We observe that while in Ag₁₄₇ and larger nanoparticles a distinct plasmon resonance is formed from the superposition of single-electron transitions, in the small Ag₅₅ nanoparticle individual single-electron transitions still have a strong effect on the plasmonic response and cause the splitting of the plasmon resonance.

The structure of the article is as follows. In Sec. II we derive the linear response of the time-dependent density matrix in the KS electron-hole space. We review the formulation of the same quantity in the Casida ap-

proach and describe the decomposition of the photo-absorption spectrum in KS electron-hole contributions. In Sec. III we benchmark the numerical accuracy of the implemented method by analyzing the KS decomposition of small benzene derivatives using both the real-time-propagation and the Casida method. This is followed by an analysis of the plasmonic response of large silver nanoparticles, which yields microscopic insight into the plasmon formation in nanoparticles. In Sec. IV we discuss the general features of the presented methodology. Our work is concluded in Sec. V.

II. METHODS

A. Linear response of the density matrix in the real-time propagation method

The time-dependent Kohn–Sham equation is defined as

$$i \frac{\partial}{\partial t} \psi_n(\mathbf{r}, t) = H_{\text{KS}}(t) \psi_n(\mathbf{r}, t), \quad (1)$$

where $H_{\text{KS}}(t)$ is the time-dependent KS Hamiltonian and $\psi_n(\mathbf{r}, t)$ is a KS wave function. The density matrix operator is defined as

$$\rho(t) = \sum_n |\psi_n(t)\rangle f_n \langle \psi_n(t)|, \quad (2)$$

where f_n is an occupation factor of the n th KS state. In order to proceed with KS decomposition, we express the density matrix in the KS basis, spanned by the ground-state KS orbitals $\psi_n^{(0)}(\mathbf{r})$, which fulfill the ground-state KS equation

$$H_{\text{KS}}^{(0)} \psi_n^{(0)}(\mathbf{r}) = \epsilon_n \psi_n^{(0)}(\mathbf{r}), \quad (3)$$

where $H_{\text{KS}}^{(0)}$ is the ground-state KS Hamiltonian and ϵ_n the KS eigenvalue of n th state. The density matrix can be written in this KS basis as

$$\begin{aligned} \rho_{nn'}(t) &= \langle \psi_n^{(0)} | \rho(t) | \psi_{n'}^{(0)} \rangle \\ &= \sum_m \langle \psi_n^{(0)} | \psi_m(t) \rangle f_m \langle \psi_m(t) | \psi_{n'}^{(0)} \rangle. \end{aligned} \quad (4)$$

This equation establishes a link between a time-dependent density matrix and the usual KS (electron-hole) basis set used in linear-response calculations, see Sec. II B. Previously, similar or related quantities have been used within the real-time propagation method for analysing the response.^{45–47,85–88}

When the real-time propagation method is applied in the linear-response regime, the usual approach is to use a δ -pulse perturbation.^{82,83} This corresponds to the Hamiltonian

$$H_{\text{KS}}(t) = H_{\text{KS}}^{(0)} + z K_z \delta(t), \quad (5)$$

where the interaction with external electromagnetic radiation is taken within the dipole approximation. The electric field is assumed to be aligned along the z direction and the constant K_z is proportional to the external electric field strength, which is assumed to be small enough to induce only negligible non-linear effects. After the perturbation by the δ -pulse at $t = 0$, Eq. (1) is propagated in time and the quantities of interest are recorded during the propagation. As a post-processing step time-domain quantities, *e.g.*, $\rho_{nn'}(t)$, can be Fourier transformed into the frequency domain.

It is important to note that the size of the density matrix $\rho_{nn'}(t)$ can be significantly reduced since only its electron-hole part is required in linear-response theory.^{75,77} It is thus sufficient to consider only $\rho_{ia}(t)$, where i and a represent occupied and unoccupied KS states, respectively. Then, we obtain the linear-response of the density matrix in electron-hole space as

$$\delta \rho_{ia}^z(\omega) = \frac{1}{K_z} \int_0^\infty [\rho_{ia}^z(t) - \rho_{ia}(0^-)] e^{i\omega t} dt + \mathcal{O}(K_z), \quad (6)$$

where $\rho_{ia}(0^-)$ is the initial density matrix before the δ -pulse perturbation and the superscript z indicates the direction of the perturbation.

In common TDDFT implementations, there is no mechanism for energy dissipation and the lifetime of excitations is infinite. A customary way to restore a finite lifetime is to apply the substitution $\omega \rightarrow \omega + i\eta$, where the parameter η is small. This leads to an exponentially decaying term in the integrand in Eq. (6), *i.e.*, $e^{i\omega t} \rightarrow e^{i\omega t} e^{-\eta t}$, and to the Lorentzian line shapes in the frequency domain. The decaying integrand also means that a finite propagation time is sufficient in practical calculations. The Gaussian line shapes can be obtained by replacing the Lorentzian decay $e^{-\eta t}$ with the Gaussian decay function $e^{-(\sigma t)^2/2}$, where the parameter σ determines the spectral line width.

Implementation

We have implemented the density matrix formalism outlined above in the RT-TDDFT code⁷¹ that is part of the open source GPAW package.^{93–95} Our implementation uses the LCAO basis set⁹² and the projector-augmented wave (PAW)⁹⁶ method. In the LCAO method the wave function $\psi_n(\mathbf{r}, t)$ is expanded in localized basis functions $\phi_\mu(\mathbf{r})$ centered at atomic coordinates

$$\psi_n(\mathbf{r}, t) = \sum_\mu \phi_\mu(\mathbf{r}) C_{\mu n}(t) \quad (7)$$

with expansion coefficients $C_{\mu n}(t)$. The density matrix is reads in the LCAO basis set as

$$\rho_{\mu\nu}(t) = \sum_n C_{\mu n}(t) f_n C_{\nu n}^*(t). \quad (8)$$

Then, Eq. (4) can be written in LCAO formalism as (using implied summation over repeated indices)

$$\rho_{nn'}(t) = C_{\mu n}^{(0)*} S_{\mu\mu'} \rho_{\mu'\nu'}(t) S_{\nu\nu'}^* C_{\nu n'}^{(0)}, \quad (9)$$

where $S_{\mu\mu'} = \int \phi_{\mu}^*(\mathbf{r}) \phi_{\mu'}(\mathbf{r}) d\mathbf{r}$ is the overlap integral of the basis functions. A detailed derivation of Eq. (9) is given in Appendix, in which it is shown that the PAW transformation affects only the evaluation of the overlap integral.

The emphasis in our implementation is to minimize the computational footprint of the analysis methods. Thus, instead of calculating Eq. (9) at every time step during the time propagation, we only store the already-calculated matrix $C_{\mu n}^z(t)$ at every time step. Then, as a post-processing step, we calculate $\rho_{\mu\nu}^z(t)$ with Eq. (8) and Fourier transform the result to obtain $\delta\rho_{\mu\nu}^z(\omega)$. The latter quantity can be subsequently transformed to $\delta\rho_{ia}^z(\omega)$ via Eq. (9) keeping only the electron-hole part. Thus, in practical implementation, the linearity of the equations allows exchanging the order of Fourier transformation and matrix multiplications.

Finally, we note that in our experience it is advantageous to store the whole time-dependent evolution of the system, *i.e.*, $C_{\mu n}^z(t)$, as done in the present implementation. While alternative on-the-fly Fourier or other transformations would reduce the amount of required storage space, they would restrict the analysis to the set of parameters specified at the outset of the calculation.

B. Linear response of the density matrix in the Casida method

In Casida's linear-response formulation of TDDFT^{75,77} the response is obtained by solving the matrix eigenvalue equation

$$\mathbf{\Omega} \mathbf{F}_I = \omega_I^2 \mathbf{F}_I \quad (10)$$

yielding excitation energies ω_I and corresponding Casida eigenvectors \mathbf{F}_I . The matrix $\mathbf{\Omega}$ is constructed in the KS electron-hole space. Using a double-index ia (jb) to denote a KS excitation from an occupied state i (j) to an unoccupied state a (b), the elements of the matrix can be written as

$$\Omega_{ia,jb} = f_{ia}^2 \delta_{ia,jb} + 2\sqrt{f_{ia}\omega_{ia}} K_{ia,jb} \sqrt{f_{jb}\omega_{jb}}, \quad (11)$$

where $f_{ia} = f_a - f_i$ is the occupation number difference, $\omega_{ia} = \epsilon_a - \epsilon_i$ is the KS eigenvalue difference, see Eq. (3), and the matrix $K_{ia,jb}$ represents the coupling between the excitations $i \rightarrow a$ and $j \rightarrow b$.⁷⁵

The linear response of the density matrix at frequency ω can be obtained as⁷⁵

$$\delta\rho_{ia}^z(\omega) = \sum_{jb}^{\text{eh}} \sqrt{f_{ia}\omega_{ia}} (\mathbf{\Omega} - \omega^2 \mathbf{1})_{ia,jb}^{-1} \sqrt{f_{jb}\omega_{jb}} \mu_{jb}^z, \quad (12)$$

where the summation runs over electron-hole pairs (eh) and involves the dipole matrix elements $\mu_{jb}^z = -\int \psi_b^{(0)*}(\mathbf{r}) z \psi_j^{(0)}(\mathbf{r}) d\mathbf{r}$. Using the spectral decomposition⁷⁵ $(\mathbf{\Omega} - \omega^2 \mathbf{1})_{ia,jb}^{-1} = \sum_I F_{I,ia} G_I(\omega) F_{I,jb}^*$, where $G_I(\omega) = 1/(\omega_I^2 - \omega^2)$, allows us to write Eq. (12) as

$$\delta\rho_{ia}^z(\omega) = \sqrt{f_{ia}\omega_{ia}} \sum_I F_{I,ia} G_I(\omega) \sum_{jb}^{\text{eh}} F_{I,jb}^* \sqrt{f_{jb}\omega_{jb}} \mu_{jb}^z. \quad (13)$$

The term $G_I(\omega)$ is divergent at excitation energies ω_I in the common TDDFT implementations due to the infinite lifetime of the excitations. Analogously to the time domain, a finite lifetime for the excitations can be restored by the substitution $\omega \rightarrow \omega + i\eta$, where the arbitrary parameter η determines the lifetime. This leads to a Lorentzian line shape and the imaginary part is given by

$$\text{Im}[G_I(\omega)] = \frac{\pi}{2\omega_I} [L(\omega) - L(-\omega)], \quad (14)$$

where $L(\omega) = 1/\pi \cdot \eta/[(\omega - \omega_I)^2 + \eta^2]$ is the Lorentzian function. Alternatively, the Gaussian line shape can be obtained by using the Gaussian function $g(\omega) = 1/\sqrt{2\pi}\sigma \cdot \exp[-(\omega - \omega_I)^2/2\sigma^2]$ instead of the Lorentzian function $L(\omega)$ in Eq. (14).

C. Kohn–Sham decomposition

The linear response of the density matrix in the KS electron-hole space, $\delta\rho_{ia}^z(\omega)$, can be calculated equivalently using both the real-time propagation [Eq. (6)] and the Casida approach [Eq. (13)]. While this quantity would already allow the analysis of the response at frequency ω in terms of its components in the KS electron-hole space, a more intuitive analysis can be obtained by connecting $\delta\rho_{ia}^z(\omega)$ to an observable photo-absorption cross-section describing the resonances of the system. First, the dynamical polarizability is given by⁷⁵

$$\alpha_{xz}(\omega) = 2 \sum_{ia}^{\text{eh}} \mu_{ia}^{x*} \delta\rho_{ia}^z(\omega). \quad (15)$$

and the photo-absorption is described the dipole strength function

$$S_z(\omega) = \frac{2\omega}{\pi} \text{Im}[\alpha_{zz}(\omega)], \quad (16)$$

which is normalized to integrate to the number of electrons in the system N_e , *i.e.*, $\int_0^\infty S_z(\omega) d\omega = N_e$. This is similar to the sum rule $\sum_I f_I^z = N_e$, where $f_I^z = 2 |\sum_{ia} \mu_{ia}^{z*} \sqrt{f_{ia}\omega_{ia}} F_{I,ia}|^2$ is the oscillator strength of the discrete excitation I .⁷⁵

By comparing Eqs. (15) and (16), we can now define the KS decomposition of the absorption spectrum as

$$S_{ia}^z(\omega) = \frac{4\omega}{\pi} \text{Im} [\mu_{ia}^{z*} \delta\rho_{ia}^z(\omega)]. \quad (17)$$

This quantity is used to analyze the response of silver nanoparticles in Sec. III B below. Previously, similar photo-absorption decompositions have been used in the electron-hole space⁸⁸ and based on, *e.g.*, spatial location^{74,89} or angular momentum.⁷⁴

III. RESULTS

A. Benzene derivatives

To benchmark the presented methods and their computational implementation, we now analyze the optical response of the molecular systems benzene (C_6H_6), naphthalene (C_{10}H_8), and anthracene ($\text{C}_{14}\text{H}_{10}$) using both the RT-TDDFT and Casida implementations in GPAW package.^{93–95,97} These characteristic conjugated molecules are suited for the present benchmark as they have well-defined $\pi \rightarrow \pi^*$ transitions that exhibit a systematic red-shift as the extent of the conjugated π -system increases.^{98,99}

As the real-time propagation uses the full time-dependent Hamiltonian matrices, the end result includes contributions from all electron-hole pairs and the limit of the full KS space is automatically achieved by propagating only the occupied orbitals. This is in contrast to the GPAW implementation of the Casida approach,⁹⁷ which commonly requires setting an energy cut-off that determines the KS transitions included in the calculation of the Casida matrix. In order to ensure comparability of the results, we have included in the calculation of the Casida matrix all the transitions that are possible within the KS electron-hole space spanned by the orbitals.

Both the RT-TDDFT and Casida calculations were carried out using the default PAW data sets and the default double- ζ polarized (dzp) basis sets within the LCAO description. While these dzp basis sets might not be sufficient for yielding numerical values at the complete-basis-set limit,^{92,100} they are suitable for qualitative analyses and for the benchmarking study presented here. The Perdew-Burke-Ernzerhof (PBE)¹⁰¹ exchange-correlation functional was employed in the adiabatic limit. A coarse grid spacing of 0.3 Å was chosen to represent densities and potentials and the molecules were surrounded by a vacuum region of at least 6 Å. The Hartree potential was evaluated with a multigrid Poisson solver using the monopole and dipole corrections for the potential.

For the RT-TDDFT calculations, we used a small time step of $\Delta t = 5$ as in order to achieve high numerical accuracy. The total propagation time was $T = 30$ fs, which is sufficient for the used Gaussian broadening with $\sigma = 0.07$ eV corresponding to a full width at half-maximum (FWHM) of 0.16 eV.

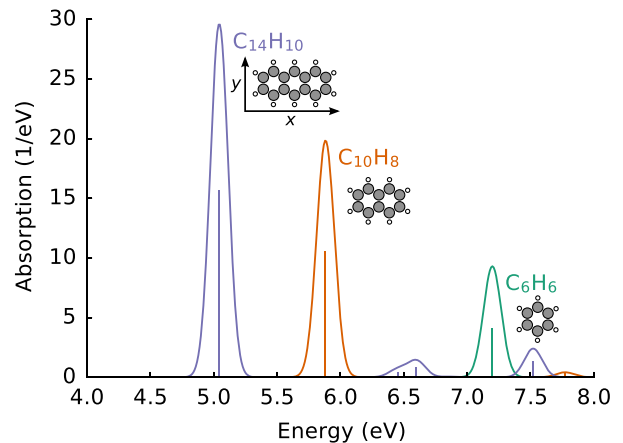


FIG. 1. Photo-absorption spectra $S_x(\omega)$ along the long axis (x) of the benzene derivatives.

The calculated photo-absorption spectra of the benzene derivatives are shown in Fig. 1. The Casida and RT-TDDFT methods yield virtually indistinguishable spectra. For conciseness, we only present an analysis for excitations along the long axis (x) of the molecules. Note, however, that the response in the other directions can be analyzed in similar fashion.

Casida approach

The response of each of the molecules is dominated by a single absorption peak (see Fig. 1), which results from discrete excitations. In Table I, we show the KS decomposition of these excitations as described by the components of the normalized Casida eigenvectors $F_{I,ia}$. Due to the normalization, $\sum_{ia} F_{I,ia}^2 = 1$ for each excitation I .

For benzene (C_6H_6 , point group D_{6h}) the excitation at 7.2 eV corresponds to the first E_{1u} transition from the doubly degenerate highest occupied molecular orbital (HOMO; E_{1g}) to the doubly degenerate lowest unoccupied molecular orbital (LUMO; E_{2u}). In the present calculations the symmetry of the molecule has not been enforced and the orbitals $\pi_{-0/1}$ and $\pi_{+0/1}^*$ span the E_{1g} and E_{2u} symmetries, respectively. Implementation-dependent numerical factors slightly lift their degeneracy and determine the exact unitary rotation between the states.

Naphthalene (C_{10}H_8) and anthracene ($\text{C}_{14}\text{H}_{10}$) belong to the D_{2h} symmetry point group. In both molecules the most prominent excitation is the B_{3u} transition, which is mainly composed of transitions from HOMO to LUMO+1 and HOMO-1 to LUMO. While in naphthalene the other contributions amount to less than 1%, in anthracene, a minor contribution originates also from a transition from HOMO-4 to LUMO+2.

TABLE I. Casida analysis of the most prominent excitations of benzene (C₆H₆), naphthalene (C₁₀H₈), and naphthalene (C₁₄H₁₀). Orbitals are enumerated with respect to HOMO (π_{-0}) and LUMO (π_{+0}^*). The orbital characters are given in brackets based on the point groups D_{6h} (benzene) and D_{2h} (naphthalene, anthracene).

Molecule	ω_I (eV)	f_I^x	$i \rightarrow a$	$F_{I,ia}^2$
C ₆ H ₆	7.198	0.2784	$\pi_{-1}(\text{E}_{1g}) \rightarrow \pi_{+1}^*(\text{E}_{2u})$	0.31430
			$\pi_{-0}(\text{E}_{1g}) \rightarrow \pi_{+0}^*(\text{E}_{2u})$	0.31254
			$\pi_{-1}(\text{E}_{1g}) \rightarrow \pi_{+0}^*(\text{E}_{2u})$	0.16863
	7.199	1.3546	$\pi_{-0}(\text{E}_{1g}) \rightarrow \pi_{+1}^*(\text{E}_{2u})$	0.16833
			$\pi_{-1}(\text{E}_{1g}) \rightarrow \pi_{+0}^*(\text{E}_{2u})$	0.31362
			$\pi_{-0}(\text{E}_{1g}) \rightarrow \pi_{+1}^*(\text{E}_{2u})$	0.31325
C ₁₀ H ₈	5.883	3.4839	$\pi_{-1}(\text{E}_{1g}) \rightarrow \pi_{+1}^*(\text{E}_{2u})$	0.16895
			$\pi_{-0}(\text{E}_{1g}) \rightarrow \pi_{+0}^*(\text{E}_{2u})$	0.16793
			$\pi_{-0}(\text{A}_u) \rightarrow \pi_{+1}^*(\text{B}_{3g})$	0.48451
C ₁₄ H ₁₀	5.044	5.2000	$\pi_{-1}(\text{B}_{2u}) \rightarrow \pi_{+0}^*(\text{B}_{1g})$	0.47748
			$\pi_{-0}(\text{B}_{3g}) \rightarrow \pi_{+1}^*(\text{A}_u)$	0.50237
			$\pi_{-1}(\text{B}_{2g}) \rightarrow \pi_{+0}^*(\text{B}_{1u})$	0.45773
			$\pi_{-4}(\text{B}_{1u}) \rightarrow \pi_{+2}^*(\text{B}_{2g})$	0.01049

RT-TDDFT approach

The Casida eigenvector $F_{I,ia}$ considered in Table I is directly related to the linear response of the density matrix, see Eq. (13), and is employed here for benchmarking the RT-TDDFT methodology described Sec. II A. In order to proceed with comparison, consider a discrete excitation J that is energetically separated from other excitations. Since $\text{Im}[G_I(\omega_J)]$ in Eq. (14) is approximately zero when $I \neq J$, only the excitation J contributes in Eq. (13). This implies that $\text{Im}[\rho_{ia}^x(\omega_J)] \approx A\sqrt{f_{ia}\omega_{ia}}F_{J,ia}$, where A is a constant independent of index ia . Thus, after normalization, $\text{Im}[\rho_{ia}^x(\omega_J)]/\sqrt{f_{ia}\omega_{ia}} \equiv F_{ia}^x(\omega_J)$ yields the components of the Casida eigenvector $F_{J,ia}$. This connection allows us to calculate the Casida eigenvector also from the RT-TDDFT approach. This is demonstrated in Table II, in which we show the calculated KS decompositions at the peak energies of the photo-absorption spectrum (Fig. 1).

In the case of benzene (C₆H₆), we inevitably obtain a superposition of the two underlying degenerate excitations (see Table I). We can, however, calculate the equivalent superimposed $F_{ia}^x(\omega)$ eigenvector also from the Casida approach (shown in the last column of Table II). For this quantity, we obtain an excellent match between the RT-TDDFT and Casida approaches.

For naphthalene (C₁₀H₈) and anthracene (C₁₄H₁₀), a single excitation dominates the response and $F_{I,ia}^2$ and $[F_{ia}^x(\omega)]^2$ should yield the same decomposition as discussed above. Indeed, we observe that the RT-TDDFT calculations of the decomposition $[F_{ia}^x(\omega)]^2$ reproduce the discrete Casida eigenvector $F_{I,ia}^2$ with very good numerical accuracy. When both $F_{I,ia}^2$ and $[F_{ia}^x(\omega)]^2$ are calculated with the Casida approach, their values should be identical if the excitation is completely isolated. While for naphthalene, these quantities are exactly the same up

TABLE II. RT-TDDFT analysis at the peak energies ω of benzene (C₆H₆), naphthalene (C₁₀H₈), and naphthalene (C₁₄H₁₀). The intensities $S_x(\omega)$ have been multiplied with the area under the peak to facilitate a comparison with the oscillator strengths f_I^x shown in Table I. The last column shows for reference $[F_{ia}^x(\omega)]^2$ as calculated with the Casida approach.

Molecule	ω (eV)	$S_x(\omega)$	$i \rightarrow a$	$[F_{ia}^x(\omega)]^2$	Casida
C ₆ H ₆	7.20	1.6283	$\pi_{-1} \rightarrow \pi_{+0}^*$	0.46184	0.46186
			$\pi_{-0} \rightarrow \pi_{+1}^*$	0.46126	0.46126
			$\pi_{-1} \rightarrow \pi_{+1}^*$	0.02045	0.02043
			$\pi_{-0} \rightarrow \pi_{+0}^*$	0.02032	0.02030
C ₁₀ H ₈	5.88	3.4776	$\pi_{-0} \rightarrow \pi_{+1}^*$	0.48472	0.48451
			$\pi_{-1} \rightarrow \pi_{+0}^*$	0.47728	0.47748
C ₁₄ H ₁₀	5.04	5.1903	$\pi_{-0} \rightarrow \pi_{+1}^*$	0.50277	0.50241
			$\pi_{-1} \rightarrow \pi_{+0}^*$	0.45745	0.45777
			$\pi_{-4} \rightarrow \pi_{+2}^*$	0.01044	0.01049

to the shown number of digits (compare the last columns of Tables I and II), for anthracene, the numerical values differ slightly. This deviation is due to a small contribution from a weak excitation that is close in energy ($\omega_I = 5.051$ eV, $f_I^x = 5 \cdot 10^{-4}$) to the dominant excitation of the anthracene molecule.

B. Silver nanoparticles

TDDFT calculations of noble metal nanoparticles up to diameters of several nanometers are computationally demanding, but they have become feasible with recent developments.^{70–74} Here, we focus on silver nanoparticles as prototypical nanoplasmonic systems with a strong plasmonic response in the visible–ultraviolet light regime.^{58,59} Using the methodology described above in conjunction with a recent RT-TDDFT implementation,⁷¹ we can analyze the response of silver nanoparticles with reasonable computational resources. For illustration, a full real-time propagation of 3000 time steps for Ag₅₆₁ can be realized in 110 hours using 144 cores on an Intel Haswell based architecture.¹⁰²

Kuisma *et al.* have previously studied icosahedral silver nanoparticles composed of 55, 147, 309, and 561 atoms corresponding to diameters ranging from 1.1 nm to 2.7 nm.⁷¹ Here, we consider the same nanoparticle series and use the same geometries and computational parameters as in Ref. 71. We employ optimized LCAO basis sets⁷¹ and the orbital-dependent Gritsenko-van Leeuwen-van Lenthe-Baerends (GLLB)¹⁰³ exchange-correlation potential with the solid-state modification by Kuisma *et al.* (GLLB-SC),¹⁰⁴ which yields an accurate description of the d electron states in noble metals.^{71,105,106}

The calculated photo-absorption spectra of the nanoparticles are shown in Fig. 2. The non-interacting-electron spectra calculated from the KS eigenvalue differences ω_{ia} and transition dipole matrix elements μ_{ia}^x

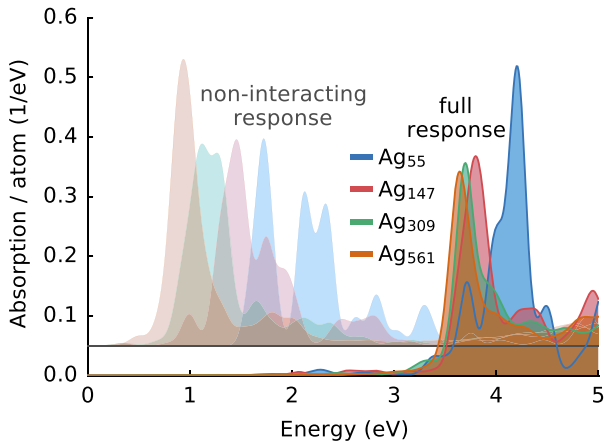


FIG. 2. Photo-absorption spectra of icosahedral silver nanoparticles. The non-interacting-electron spectra shown for comparison are vertically shifted and scaled by a factor of 0.2.

are also shown to facilitate the discussion below. In Ref. 71 it was observed that the plasmon resonance is well-formed in Ag_{147} and in larger nanoparticles, whereas the response of Ag_{55} consists of multiple peaks, the origin of which cannot be readily resolved. In the following, we analyze the response of nanoparticles in terms of the KS decomposition, which enables us to shed light on the response of the Ag_{55} nanoparticle.

Transition contribution maps

In order to analyze the response in terms of the Kohn–Sham decomposition, we present the decomposition as a transition contribution map (TCM; see Fig. 3 below),^{40,107} which is an especially useful representation for plasmonic systems in which resonances are typically superpositions of many electron-hole excitations. The TCM represents the KS decomposition weight $w_{ia}(\omega)$ at a fixed ω in the two-dimensional (2D) plane spanned by the energy axes for occupied and unoccupied states. More specifically, the 2D plot is defined by

$$M_{\omega}^{\text{TCM}}(\varepsilon_o, \varepsilon_u) = \sum_{ia} w_{ia}(\omega) g_{ia}(\varepsilon_o, \varepsilon_u), \quad (18)$$

where g_{ia} is a 2D broadening function of the discrete KS states. Here, we employ the Gaussian function

$$g_{ia}(\varepsilon_o, \varepsilon_u) = (\sqrt{2\pi}\sigma)^{-2} e^{-\frac{(\varepsilon_o - \varepsilon_i)^2 + (\varepsilon_u - \varepsilon_a)^2}{2\sigma^2}} \quad (19)$$

with $\sigma = 0.07$ eV. The same σ parameter is also used in the spectral broadening. For the weight $w_{ia}(\omega)$, we use the absorption decomposition of Eq. (17) normalized by the total absorption, *i.e.*,

$$w_{ia}(\omega) = S_{ia}^x(\omega) / S_x(\omega). \quad (20)$$

Due to the icosahedral symmetry of the nanoparticles their response is isotropic, $S_x(\omega) = S_y(\omega) = S_z(\omega)$, and the decomposition is degenerate (compare the case of benzene in Sec. III A).

Alternatively, instead of Eq. (20) one could use, *e.g.*, the normalized transition density matrix ($w_{ia}(\omega) = |\rho_{ia}^x(\omega)|^2$) as the weight. Equation (20), however, has the advantage that it retains the information about the sign of the response in the KS decomposition and has a physically sound interpretation as the photo-absorption decomposition.

TCMs of the nanoparticles at different resonance energies are shown in Fig. 3 along with the density of states (DOS), which has been colored to indicate the *sp* and *d* character of the states. The latter decomposition is based on the angular momentum quantum number l_{μ} of the LCAO basis functions indexed by μ . For example, the *d* character of the n th state is estimated as $\sum_{\mu: l_{\mu}=2} |C_{\mu n}^{(0)}|^2$, where the coefficients are normalized such that $\sum_{\mu} |C_{\mu n}^{(0)}|^2 = 1$.

Analysis of Ag_{147} , Ag_{309} , and Ag_{561}

First, we consider the largest nanoparticles Ag_{147} , Ag_{309} , and Ag_{561} , the TCMs of which are shown in Figs. 3(d–f). The TCMs highlight two major features in their response. First, there is a strong positive constructive contribution⁴¹ (red features in Fig. 3) from the KS transitions whose eigenvalue differences are significantly lower than the plasmon resonance energy ω . The same low-energy *sp* transitions are responsible for the strong peaks in the non-interacting-electron spectra (see Fig. 2), which are indicated in Fig. 3 by dashed lines. Thus, TCM shows how the resonance energy is blue-shifted as the interaction is turned on from the non-interacting case ($\lambda = 0$) to the fully interacting one ($\lambda = 1$). This demonstrates the plasmonic nature of the excitation in the so-called λ -scaling approach for plasmon identification,^{39,108} and illustrates the importance of low-energy transitions for plasmon formation.⁴⁷ Another prominent feature in the response is the damping due to *d* electrons, which is seen in the TCMs as large negative contributions from occupied *d* states into unoccupied states (blue features at $\varepsilon_o \approx -4$ eV in Fig. 3). Interestingly, the plasmon peak appears close to the onset of *d* electron transitions, corresponding to the intersection of the line $\varepsilon_u - \varepsilon_o = \omega$ and the horizontal Fermi level line. Generally, with increasing nanoparticle size the DOS becomes increasingly continuous, which is also visible in the increasing uniformity of the TCMs.

In Ref. 73, TCMs for charged silver nanoparticles up to Ag_{309} have been studied. The two main features in Fig. 3, the low-energy *sp* transitions and the *d* electron damping, are in agreement with these TCMs reported earlier. In contrast to Fig. 3, the TCMs in Ref. 73 show, however, also a significant contribution from *sp* transitions close

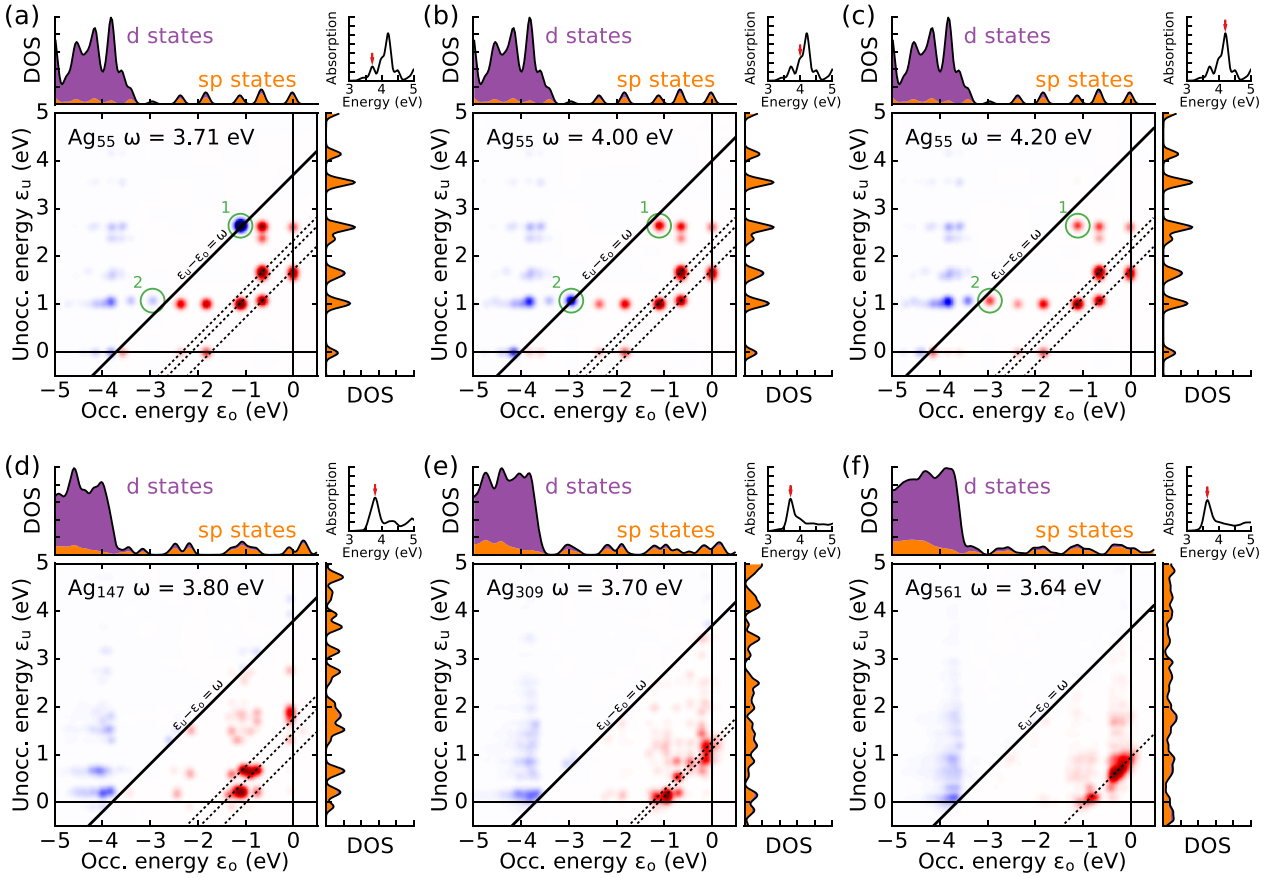


FIG. 3. Transition contribution maps for the photo-absorption decomposition of Ag_{55} at different resonance energies ω (a–c), and those of Ag_{147} (d), Ag_{309} (e), and Ag_{561} (f) at the respective plasmon resonance energies. The KS eigenvalues are given with respect to the Fermi level. The constant transition energy lines $\varepsilon_u - \varepsilon_o = \omega$ are superimposed at the analysis energy (solid line) and at the resonance energies of the non-interacting-electron spectra (dashed lines, see Fig. 2). Red and blue colors indicate positive and negative values of the photo-absorption decomposition, respectively. The inset of each panel shows the absorption spectrum with the arrow pointing at the analysis frequency ω . The densities of states (DOS) have been colored to indicate sp and d character of the states. The transitions marked with green circles in panels (a–c) are discussed in the text.

to the $\varepsilon_u - \varepsilon_o = \omega$ line. We consider this to be due to the different choice of the TCM weight $w_{ia}(\omega)$ in Ref. 73. In the absorption decomposition we used in Fig. 3 [Eqs. (17) and (20)] the KS components are essentially weighted with the dipole matrix element μ_{ia}^x , which affects the relative magnitudes observed in TCM.

Analysis of Ag_{55}

Next, we consider the Ag_{55} nanoparticle that exhibits multiple strong peaks in the absorption spectrum, resulting in difficulties in identifying the plasmon resonance. The TCM analyses for the three prominent peak energies are shown in Figs. 3(a–c). Due to its small size, Ag_{55} has well defined, discrete KS states as visible in DOS. The overall features in TCMs are similar to those of the larger nanoparticles, *i.e.*, the low-energy sp transitions and the d electron transitions yield positive and negative contributions, respectively, though the low-energy transitions

that form the plasmon are energetically clearly separated.

In contrast to the larger nanoparticles, in the Ag_{55} nanoparticle some of the strongly contributing sp transitions are located close to the peak frequencies, *i.e.*, close to the $\varepsilon_u - \varepsilon_o = \omega$ lines in the TCMs. These excitations are marked in Figs. 3(a–c) by green circles numbered as 1 and 2. By examining these KS transitions as a function of frequency ω (TCMs with the 0.01 eV resolution are provided as Supplemental Material¹⁰⁹), we note that the first transition changes its sign at $\omega = 3.85$ eV, close to the minimum between the peak maxima at 3.71 eV [Fig. 3(a)] and 4.00 eV (b). Similarly, the second transition changes its sign at $\omega = 4.06$ eV between the maxima at 4.00 eV (b) and 4.20 eV (c). At the same time, the low-energy transitions forming the plasmon remain mainly unchanged over this frequency window. Thus, the presence of multiple peaks in the Ag_{55} spectrum seems to correspond to a strong coupling between the marked KS transitions and the plasmon. This is seen as the splitting of the plasmon into multiple resonances with antisym-

metric and symmetric combinations of the KS transition and the plasmonic transitions. In the larger nanoparticles, the interaction between the plasmon and the nearby KS transitions is weak and the coupling is merely seen as a broadening of the plasmon peak.

A detailed inspection reveals that some d electron transitions also change their sign in the frequency range where the peak splitting occurs. The changes in their sign, however, do not match the maxima and minima of the absorption spectrum like in the case of the marked KS transitions. Thus, we expect the marked sp transitions to be the major cause for the plasmon splitting.

In the literature, Ag₅₅ has been reported to have slightly varying spectra depending, *e.g.*, on the exact geometry, the exchange-correlation functional, and the numerical parameters used.^{14,47,73,74,100,110,111} Correspondingly, the electronic structures are different and the Ag₅₅ spectra have single or multiple peaks. We expect, however, that the splitting behavior observed here can be a useful general concept for understanding the response of small plasmonic nanoparticles.

IV. DISCUSSION

The RT-TDDFT approach provides a more favorable scaling with the system size than the Casida approach. The latter, however, achieves a smaller pre-factor, especially when using non-local (*e.g.*, hybrid exchange-correlation functionals),⁸⁴ which renders it computationally more efficient for small and moderately-sized systems. In contrast, the RT-TDDFT approach becomes very attractive for systems comprising thousands of electrons (and typically hundreds of atoms) such as the silver nanoparticles considered in the present work. Previously, the lack of a decomposition scheme on par with the Casida method has been identified as a drawback of the RT-TDDFT approach.⁸⁴ Here, we have introduced and demonstrated the performance of a method that overcomes this limitation and represents an efficient tool for analyzing electronic excitations within RT-TDDFT in general, and plasmonic response in particular.

It should be noted that in the RT-TDDFT approach the observable response is sensitive to the external perturbation used to initialize the time propagation. If the perturbation is chosen to be, say, a dipole perturbation along the x direction, only excitations with a dipole component parallel to x are observable in the response. By combining at most three separate time-propagation calculations (possibly even less in the cases of higher symmetry) with dipole perturbations along the x , y , and z axes, one can recover the full dynamical polarizability tensor. However, for obtaining optically dark (dipole-forbidden) excitations from RT-TDDFT calculations, one would need to run the time propagation with different initial perturbations. This is in contrast to the Casida approach, where also dipole-forbidden excitations are obtained by diagonalizing the Ω matrix.

It was illustrated in Sec. III A that the RT-TDDFT method does not yield direct access to the discrete spectrum, but rather allows an analysis at chosen frequencies yielding the combined response coming from all the contributing discrete excitations. Usually, this is not a significant restriction as in experimental measurements the energy resolution is limited by instrumental broadening and the excitation lifetimes. Computationally, the energy resolution is determined by the broadening parameter, which can be always reduced by increasing the propagation time. Furthermore, for larger systems that are the primary application area for RT-TDDFT, the electronic spectrum becomes increasingly dense and the distinction of individual excitations is less relevant.

V. CONCLUSIONS

In this work we have presented that the linear response of the density matrix in the Kohn–Sham electron-hole basis can be obtained from real-time propagation TDDFT via a basis transformation. The methodology has been implemented in a recent RT-TDDFT code⁷¹ and is to be made publicly available as a part of the open source electronic structure code GPAW.^{93–95}

The present approach provides access to the same information via RT-TDDFT that is usually available only with the Casida approach. This was specifically demonstrated by a careful comparison of the results for benzene derivatives, which were shown to be numerically almost identical for the Casida and RT-TDDFT calculations.

Using the presented methodology, we analyzed the plasmonic response of icosahedral silver nanoparticles in the Kohn–Sham electron-hole space. The Ag₅₅ nanoparticle was considered in detail and the multiple resonances in its response were shown to reflect the splitting of the plasmon due to the strong coupling between the plasmon and individual single-electron transitions. In the larger Ag₁₄₇, Ag₃₀₉, and Ag₅₆₁ nanoparticles, the interaction between plasmon and individual single-electron transitions close to the resonance is weaker and a distinct plasmon resonance emerges from the constructive superposition of the low-energy Kohn–Sham transitions^{39,47,108} accompanied by the damping due to d electron transitions.

In summary, the present work raises the analysis capabilities of the RT-TDDFT to the same level as with the Casida approach, without compromising the computational benefits of RT-TDDFT.

ACKNOWLEDGMENTS

We thank the Academy of Finland for support through its Centres of Excellence Programme (2012–2017) under Projects No. 251748 and No. 284621. M.K. is grateful for Academy of Finland Postdoctoral Researcher funding under Project No. 295602. T. P. R. thanks the Vilho, Yrjö

and Kalle Väisälä Foundation of the Finnish Academy of Science and Letters, and Finnish Cultural Foundation for support. We also thank the Swedish Research Council, the Knut and Alice Wallenberg Foundation, and the Swedish Foundation for Strategic Research for support. We acknowledge computational resources provided by CSC – IT Center for Science (Finland), the Aalto Science-IT project (Aalto University School of Science), the Swedish National Infrastructure for Computing at NSC (Linköping) and at PDC (Stockholm).

Appendix: Derivation of Eq. (9) within the PAW formalism

Within the PAW formalism, Eq. (1) reads

$$i\mathcal{T}^\dagger \mathcal{T} \frac{\partial}{\partial t} \tilde{\psi}_n(\mathbf{r}, t) = \mathcal{T}^\dagger H_{\text{KS}}(t) \mathcal{T} \tilde{\psi}_n(\mathbf{r}, t), \quad (\text{A.1})$$

where $\tilde{\psi}_n(\mathbf{r}, t)$ is a pseudo wave function and \mathcal{T} denotes the PAW transformation operator.⁹⁶

In the LCAO method, the pseudo wave function $\tilde{\psi}_n(\mathbf{r}, t)$ is expanded in localized basis functions $\tilde{\phi}_\mu(\mathbf{r})$ centered at atomic coordinates

$$\tilde{\psi}_n(\mathbf{r}, t) = \sum_\mu \tilde{\phi}_\mu(\mathbf{r}) C_{\mu n}(t), \quad (\text{A.2})$$

with expansion coefficients $C_{\mu n}(t)$. The corresponding all-electron wave function is given by [compare to Eq. (7)]

$$\psi_n(\mathbf{r}, t) = \mathcal{T} \tilde{\psi}_n(\mathbf{r}, t) = \sum_\mu \phi_\mu(\mathbf{r}) C_{\mu n}(t), \quad (\text{A.3})$$

where the all-electron basis functions have been defined as $\phi_\mu = \mathcal{T} \tilde{\phi}_\mu$.

The time-dependent all-electron real-space density matrix can be obtained as

$$\rho(\mathbf{r}, \mathbf{r}', t) = \sum_{\mu\nu} \phi_\mu(\mathbf{r}) \rho_{\mu\nu}(t) \phi_\nu^*(\mathbf{r}'), \quad (\text{A.4})$$

where the density matrix in the LCAO basis $\rho_{\mu\nu}(t)$ is given by Eq. (8).

The transformation of the real-space density matrix to the basis defined by the ground-state KS orbitals $\psi_n^{(0)}(\mathbf{r})$, see Eq. (3), is given by

$$\rho_{nn'}(t) = \int d\mathbf{r} \int d\mathbf{r}' \psi_n^{(0)*}(\mathbf{r}) \rho(\mathbf{r}, \mathbf{r}', t) \psi_{n'}^{(0)}(\mathbf{r}'). \quad (\text{A.5})$$

By expanding $\psi_n^{(0)}(\mathbf{r})$ in the LCAO basis as in Eq. (A.3) and inserting Eq. (A.4) into Eq. (A.5), we obtain after reordering the integrals

$$\begin{aligned} \rho_{nn'}(t) &= \sum_\mu C_{\mu n}^{(0)*} \sum_{\mu'} \underbrace{\int d\mathbf{r} \phi_\mu^*(\mathbf{r}) \phi_{\mu'}(\mathbf{r})}_{S_{\mu\mu'}} \\ &\cdot \sum_{\nu'} \rho_{\mu'\nu'}(t) \sum_\nu \underbrace{\int d\mathbf{r}' \phi_{\nu'}^*(\mathbf{r}') \phi_\nu(\mathbf{r}')}_{S_{\nu\nu'}^*} C_{\nu n'}^{(0)}. \end{aligned} \quad (\text{A.6})$$

Here, we have isolated the overlap integrals $S_{\mu\mu'}$ used regularly in LCAO calculations, *i.e.*,

$$S_{\mu\mu'} = \int d\mathbf{r} \phi_\mu^*(\mathbf{r}) \phi_{\mu'}(\mathbf{r}) = \int d\mathbf{r} \tilde{\phi}_\mu^*(\mathbf{r}) \mathcal{T}^\dagger \mathcal{T} \tilde{\phi}_{\mu'}(\mathbf{r}). \quad (\text{A.7})$$

After simplifying the overlap integrals in Eq. (A.6), we obtain Eq. (9). We note that the PAW transformation affects only the evaluation of the overlap integrals $S_{\mu\mu'}$, see Eq. (A.7).

* tuomas.rossi@alumni.aalto.fi

† mikael.j.kuisma@jyu.fi

‡ erhart@chalmers.se

¹ E. Runge and E. K. U. Gross, *Phys. Rev. Lett.* **52**, 997 (1984).

² P. Hohenberg and W. Kohn, *Phys. Rev.* **136**, B864 (1964).

³ W. Kohn and L. J. Sham, *Phys. Rev.* **140**, A1133 (1965).

⁴ M. A. L. Marques, N. T. Maitra, F. M. S. Nogueira, E. K. U. Gross, and A. Rubio, eds., *Fundamentals of Time-Dependent Density Functional Theory*, Lecture Notes in Physics, Vol. 837 (Springer, 2012).

⁵ C. A. Ullrich, *Time-Dependent Density-Functional Theory: Concepts and Applications* (Oxford University Press, 2012).

⁶ W. Ekardt, *Phys. Rev. Lett.* **52**, 1925 (1984).

⁷ M. J. Puska, R. M. Nieminen, and M. Manninen, *Phys. Rev. B* **31**, 3486 (1985).

⁸ D. E. Beck, *Phys. Rev. B* **35**, 7325 (1987).

⁹ S. M. Morton, D. W. Silverstein, and L. Jensen, *Chem. Rev.* **111**, 3962 (2011).

¹⁰ A. Varas, P. García-González, J. Feist, F. García-Vidal, and A. Rubio, *Nanophotonics* **5**, 409 (2016).

¹¹ E. Prodan, P. Nordlander, and N. J. Halas, *Nano Lett.* **3**, 1411 (2003).

¹² C. M. Aikens, S. Li, and G. C. Schatz, *J. Phys. Chem. C* **112**, 11272 (2008).

¹³ J. Zuloaga, E. Prodan, and P. Nordlander, *ACS Nano* **4**, 5269 (2010).

¹⁴ H.-C. Weissker and C. Mottet, *Phys. Rev. B* **84**, 165443 (2011).

¹⁵ J.-H. Li, M. Hayashi, and G.-Y. Guo, *Phys. Rev. B* **88**, 155437 (2013).

¹⁶ G. Piccini, R. W. A. Havenith, R. Broer, and M. Stener, *J. Phys. Chem. C* **117**, 17196 (2013).

¹⁷ R. W. Burgess and V. J. Keast, *J. Phys. Chem. C* **118**, 3194 (2014).

¹⁸ G. Barcaro, L. Sementa, A. Fortunelli, and M. Stener, *J. Phys. Chem. C* **118**, 12450 (2014).

¹⁹ H.-C. Weissker and X. Lopez-Lozano, *Phys. Chem. Chem. Phys.* **17**, 28379 (2015).

- ²⁰ G.-T. Bae and C. M. Aikens, *J. Phys. Chem. C* **119**, 23127 (2015).
- ²¹ M. Zapata Herrera, J. Aizpurua, A. K. Kazansky, and A. G. Borisov, *Langmuir* **32**, 2829 (2016).
- ²² J. Zuloaga, E. Prodan, and P. Nordlander, *Nano Lett.* **9**, 887 (2009).
- ²³ P. Song, P. Nordlander, and S. Gao, *J. Chem. Phys.* **134**, 074701 (2011).
- ²⁴ P. Song, S. Meng, P. Nordlander, and S. Gao, *Phys. Rev. B* **86**, 121410 (2012).
- ²⁵ D. Marinica, A. Kazansky, P. Nordlander, J. Aizpurua, and A. G. Borisov, *Nano Lett.* **12**, 1333 (2012).
- ²⁶ P. Zhang, J. Feist, A. Rubio, P. García-González, and F. J. García-Vidal, *Phys. Rev. B* **90**, 161407 (2014).
- ²⁷ A. Varas, P. García-González, F. J. García-Vidal, and A. Rubio, *J. Phys. Chem. Lett.* **6**, 1891 (2015).
- ²⁸ M. Barbry, P. Koval, F. Marchesin, R. Esteban, A. G. Borisov, J. Aizpurua, and D. Sánchez-Portal, *Nano Lett.* **15**, 3410 (2015).
- ²⁹ V. Kulkarni and A. Manjavacas, *ACS Photonics* **2**, 987 (2015).
- ³⁰ T. P. Rossi, A. Zugarramurdi, M. J. Puska, and R. M. Nieminen, *Phys. Rev. Lett.* **115**, 236804 (2015).
- ³¹ F. Marchesin, P. Koval, M. Barbry, J. Aizpurua, and D. Sánchez-Portal, *ACS Photonics* **3**, 269 (2016).
- ³² T. Lahtinen, E. Hulkko, K. Sokolowska, T.-R. Tero, V. Saarnio, J. Lindgren, M. Pettersson, H. Hakkinen, and L. Lehtovaara, *Nanoscale* **8**, 18665 (2016).
- ³³ A. Manjavacas, F. Marchesin, S. Thongrattanasiri, P. Koval, P. Nordlander, D. Sánchez-Portal, and F. J. García de Abajo, *ACS Nano* **7**, 3635 (2013).
- ³⁴ K. Andersen and K. S. Thygesen, *Phys. Rev. B* **88**, 155128 (2013).
- ³⁵ K. Andersen, K. W. Jacobsen, and K. S. Thygesen, *Phys. Rev. B* **90**, 161410 (2014).
- ³⁶ A. Lauchner, A. E. Schlather, A. Manjavacas, Y. Cui, M. J. McClain, G. J. Stec, F. J. García de Abajo, P. Nordlander, and N. J. Halas, *Nano Lett.* **15**, 6208 (2015).
- ³⁷ S. Gao and Z. Yuan, *Phys. Rev. B* **72**, 121406 (2005).
- ³⁸ J. Yan, Z. Yuan, and S. Gao, *Phys. Rev. Lett.* **98**, 216602 (2007).
- ³⁹ S. Bernadotte, F. Evers, and C. R. Jacob, *J. Phys. Chem. C* **117**, 1863 (2013).
- ⁴⁰ S. Malola, L. Lehtovaara, J. Enkovaara, and H. Häkkinen, *ACS Nano* **7**, 10263 (2013).
- ⁴¹ E. B. Guidez and C. M. Aikens, *Nanoscale* **4**, 4190 (2012).
- ⁴² E. B. Guidez and C. M. Aikens, *Nanoscale* **6**, 11512 (2014).
- ⁴³ T. Yasuike, K. Nobusada, and M. Hayashi, *Phys. Rev. A* **83**, 013201 (2011).
- ⁴⁴ D. Casanova, J. M. Matxain, and J. M. Ugalde, *J. Phys. Chem. C* **120**, 12742 (2016).
- ⁴⁵ E. Townsend and G. W. Bryant, *Nano Lett.* **12**, 429 (2012).
- ⁴⁶ E. Townsend and G. W. Bryant, *J. Opt.* **16**, 114022 (2014).
- ⁴⁷ J. Ma, Z. Wang, and L.-W. Wang, *Nat. Commun.* **6**, 10107 (2015).
- ⁴⁸ L. Bursi, A. Calzolari, S. Corni, and E. Molinari, *ACS Photonics* **3**, 520 (2016).
- ⁴⁹ R. Esteban, A. G. Borisov, P. Nordlander, and J. Aizpurua, *Nat. Commun.* **3**, 825 (2012).
- ⁵⁰ L. Stella, P. Zhang, F. J. García-Vidal, A. Rubio, and P. García-González, *J. Phys. Chem. C* **117**, 8941 (2013).
- ⁵¹ X. Chen, J. E. Moore, M. Zekarias, and L. Jensen, *Nat. Commun.* **6**, 8921 (2015).
- ⁵² W. Yan, M. Wubs, and N. Asger Mortensen, *Phys. Rev. Lett.* **115**, 137403 (2015).
- ⁵³ T. V. Teperik, A. K. Kazansky, and A. G. Borisov, *Phys. Rev. B* **93**, 155431 (2016).
- ⁵⁴ C. Ciraci and F. Della Sala, *Phys. Rev. B* **93**, 205405 (2016).
- ⁵⁵ C. David, J. Christensen, and N. A. Mortensen, *Phys. Rev. B* **94**, 165410 (2016).
- ⁵⁶ T. Christensen, W. Yan, A.-P. Jauho, M. Soljacic, and N. A. Mortensen, *Phys. Rev. Lett.*, in press (2017). [arXiv:1608.05421v2](https://arxiv.org/abs/1608.05421v2).
- ⁵⁷ C. Ciraci, R. T. Hill, J. J. Mock, Y. Urzhumov, A. I. Fernández-Domínguez, S. A. Maier, J. B. Pendry, A. Chilkoti, and D. R. Smith, *Science* **337**, 1072 (2012).
- ⁵⁸ J. A. Scholl, A. L. Koh, and J. A. Dionne, *Nature* **483**, 421 (2012).
- ⁵⁹ H. Haberland, *Nature* **494**, E1 (2013).
- ⁶⁰ K. J. Savage, M. M. Hawkeye, R. Esteban, A. G. Borisov, J. Aizpurua, and J. J. Baumberg, *Nature* **491**, 574 (2012).
- ⁶¹ M. Banik, P. Z. El-Khoury, A. Nag, A. Rodriguez-Perez, N. Guarrottxena, G. C. Bazan, and V. A. Apkarian, *ACS Nano* **6**, 10343 (2012).
- ⁶² M. Banik, V. A. Apkarian, T.-H. Park, and M. Galperin, *J. Phys. Chem. Lett.* **4**, 88 (2013).
- ⁶³ J. A. Scholl, A. García-Etxarri, A. L. Koh, and J. A. Dionne, *Nano Lett.* **13**, 564 (2013).
- ⁶⁴ S. F. Tan, L. Wu, J. K. Yang, P. Bai, M. Bosman, and C. A. Nijhuis, *Science* **343**, 1496 (2014).
- ⁶⁵ C. Zhang, H. Zhao, L. Zhou, A. E. Schlather, L. Dong, M. J. McClain, D. F. Swearer, P. Nordlander, and N. J. Halas, *Nano Lett.* **16**, 6677 (2016).
- ⁶⁶ A. Sanders, R. W. Bowman, and J. J. Baumberg, *Sci. Rep.* **6**, 32988 (2016).
- ⁶⁷ J. Mertens, A. Demetriadou, R. W. Bowman, F. Benz, M.-E. Kleemann, C. Tserkezis, Y. Shi, H. Y. Yang, O. Hess, J. Aizpurua, and J. J. Baumberg, *Nano Lett.* **16**, 5605 (2016).
- ⁶⁸ M. S. Tame, K. R. McEnery, S. K. Ozdemir, J. Lee, S. A. Maier, and M. S. Kim, *Nat. Phys.* **9**, 329 (2013).
- ⁶⁹ W. Zhu, R. Esteban, A. G. Borisov, J. J. Baumberg, P. Nordlander, H. J. Lezec, J. Aizpurua, and K. B. Crozier, *Nat. Commun.* **7**, 11495 (2016).
- ⁷⁰ K. Iida, M. Noda, K. Ishimura, and K. Nobusada, *J. Phys. Chem. A* **118**, 11317 (2014).
- ⁷¹ M. Kuisma, A. Sakkó, T. P. Rossi, A. H. Larsen, J. Enkovaara, L. Lehtovaara, and T. T. Rantala, *Phys. Rev. B* **91**, 115431 (2015).
- ⁷² O. Baseggio, G. Fronzoni, and M. Stener, *J. Chem. Phys.* **143**, 024106 (2015).
- ⁷³ O. Baseggio, M. De Vetta, G. Fronzoni, M. Stener, L. Sementa, A. Fortunelli, and A. Calzolari, *J. Phys. Chem. C* **120**, 12773 (2016).
- ⁷⁴ P. Koval, F. Marchesin, D. Foerster, and D. Sánchez-Portal, *J. Phys.: Condens. Matter* **28**, 214001 (2016).
- ⁷⁵ M. E. Casida, in *Recent Advances in Density Functional Methods, Part I*, edited by D. P. Chong (World Scientific, Singapore, 1995) p. 155.
- ⁷⁶ M. Petersilka, U. J. Gossmann, and E. K. U. Gross, *Phys. Rev. Lett.* **76**, 1212 (1996).
- ⁷⁷ M. E. Casida, *J. Mol. Struct. THEOCHEM* **914**, 3 (2009).
- ⁷⁸ R. Bauernschmitt and R. Ahlrichs, *Chem. Phys. Lett.*

- 256**, 454 (1996).
- ⁷⁹ R. E. Stratmann, G. E. Scuseria, and M. J. Frisch, *J. Chem. Phys.* **109**, 8218 (1998).
- ⁸⁰ B. Walker, A. M. Saitta, R. Gebauer, and S. Baroni, *Phys. Rev. Lett.* **96**, 113001 (2006).
- ⁸¹ X. Andrade, S. Botti, M. A. L. Marques, and A. Rubio, *J. Chem. Phys.* **126**, 184106 (2007).
- ⁸² K. Yabana and G. F. Bertsch, *Phys. Rev. B* **54**, 4484 (1996).
- ⁸³ K. Yabana, T. Nakatsukasa, J.-I. Iwata, and G. F. Bertsch, *Phys. Status Solidi B* **243**, 1121 (2006).
- ⁸⁴ T. Sander and G. Kresse, *J. Chem. Phys.* **146**, 064110 (2017).
- ⁸⁵ L. Yan, F. Wang, and S. Meng, *ACS Nano* **10**, 5452 (2016).
- ⁸⁶ Y. Li and C. A. Ullrich, *Chem. Phys.* **391**, 157 (2011).
- ⁸⁷ Y. Li and C. A. Ullrich, *J. Chem. Theory Comput.* **11**, 5838 (2015).
- ⁸⁸ M. Repisky, L. Konecny, M. Kadek, S. Komorovsky, O. L. Malkin, V. G. Malkin, and K. Ruud, *J. Chem. Theory Comput.* **11**, 980 (2015).
- ⁸⁹ G. Kolesov, O. Grånäs, R. Hoyt, D. Vinichenko, and E. Kaxiras, *J. Chem. Theory Comput.* **12**, 466 (2016).
- ⁹⁰ S. Malola, L. Lehtovaara, and H. Häkkinen, *J. Phys. Chem. C* **118**, 20002 (2014).
- ⁹¹ S. Malola, M. J. Hartmann, and H. Häkkinen, *J. Phys. Chem. Lett.* **6**, 515 (2015).
- ⁹² A. H. Larsen, M. Vanin, J. J. Mortensen, K. S. Thygesen, and K. W. Jacobsen, *Phys. Rev. B* **80**, 195112 (2009).
- ⁹³ J. J. Mortensen, L. B. Hansen, and K. W. Jacobsen, *Phys. Rev. B* **71**, 035109 (2005).
- ⁹⁴ J. Enkovaara, C. Rostgaard, J. J. Mortensen, J. Chen, M. Duřak, L. Ferrighi, J. Gavnholt, C. Glinsvad, V. Haikola, H. A. Hansen, H. H. Kristoffersen, M. Kuisma, A. H. Larsen, L. Lehtovaara, M. Ljungberg, O. Lopez-Acevedo, P. G. Moses, J. Ojanen, T. Olsen, V. Petzold, N. A. Romero, J. Stausholm-Møller, M. Strange, G. A. Tritsarlis, M. Vanin, M. Walter, B. Hammer, H. Häkkinen, G. K. H. Madsen, R. M. Nieminen, J. K. Nørskov, M. Puska, T. T. Rantala, J. Schiøtz, K. S. Thygesen, and K. W. Jacobsen, *J. Phys.: Condens. Matter* **22**, 253202 (2010).
- ⁹⁵ “GPAW: DFT and beyond within the projector-augmented wave method,” <https://wiki.fysik.dtu.dk/gpaw/>.
- ⁹⁶ P. E. Blöchl, *Phys. Rev. B* **50**, 17953 (1994).
- ⁹⁷ M. Walter, H. Häkkinen, L. Lehtovaara, M. Puska, J. Enkovaara, C. Rostgaard, and J. J. Mortensen, *J. Chem. Phys.* **128**, 244101 (2008).
- ⁹⁸ P. G. Wilkinson, *Can. J. Phys.* **34**, 596 (1956).
- ⁹⁹ J. Ferguson, L. W. Reeves, and W. G. Schneider, *Can. J. Chem.* **35**, 1117 (1957).
- ¹⁰⁰ T. P. Rossi, S. Lehtola, A. Sakko, M. J. Puska, and R. M. Nieminen, *J. Chem. Phys.* **142**, 094114 (2015).
- ¹⁰¹ J. P. Perdew, K. Burke, and M. Ernzerhof, *Phys. Rev. Lett.* **77**, 3865 (1996); *Phys. Rev. Lett.* **78**, 1396 (1997).
- ¹⁰² The timing was performed on the Taito supercluster of CSC – IT Center for Science, Finland. Each computing node has Intel Haswell E5-2690v3 processors and the nodes are connected with Infiniband FDR interconnect. For further details of the hardware, see <https://research.csc.fi/taito-supercluster> (9th Feb 2017).
- ¹⁰³ O. Gritsenko, R. van Leeuwen, E. van Lenthe, and E. J. Baerends, *Phys. Rev. A* **51**, 1944 (1995).
- ¹⁰⁴ M. Kuisma, J. Ojanen, J. Enkovaara, and T. T. Rantala, *Phys. Rev. B* **82**, 115106 (2010).
- ¹⁰⁵ J. Yan, K. W. Jacobsen, and K. S. Thygesen, *Phys. Rev. B* **84**, 235430 (2011).
- ¹⁰⁶ J. Yan, K. W. Jacobsen, and K. S. Thygesen, *Phys. Rev. B* **86**, 241404 (2012).
- ¹⁰⁷ Y. He and T. Zeng, *J. Phys. Chem. C* **114**, 18023 (2010).
- ¹⁰⁸ C. M. Krauter, S. Bernadotte, C. R. Jacob, M. Pernpointner, and A. Dreuw, *J. Phys. Chem. C* **119**, 24564 (2015).
- ¹⁰⁹ See Supplemental Material for additional transition contribution maps for the Ag₅₅ nanoparticle.
- ¹¹⁰ G.-T. Bae and C. M. Aikens, *J. Phys. Chem. C* **116**, 10356 (2012).
- ¹¹¹ F. Rabilloud, *J. Chem. Phys.* **141**, 144302 (2014).